Local Mode Analysis using Windowed Fourier Transform and Wavelet Techniques

D. A. D'Ippolito and J. R. Myra

Lodestar Research Corporation, 2400 Central Avenue, Boulder, Colorado 80301

August, 2004

DOE/ER/54650-2 LRC-04-101

LODESTAR RESEARCH CORPORATION

Local Mode Analysis using Windowed Fourier Transform and Wavelet Techniques

D. A. D'Ippolito and J. R. Myra
Lodestar Research Corporation

A. Introduction and Overview

Motivated by the growing capability of numerical rf simulations, there is a need to develop appropriate post-processing tools for extracting physical information from the numerical solutions. For example, full-wave ICRF codes yield complicated rf field patterns, and the challenge is to understand these patterns by appealing to the intuitive, but approximate, physics-based notion of local plasma modes (global eigenmodes, transmitted and reflected waves, and mode conversions between different types of waves). Quantitative information on the local wavevectors, amplitudes and wave polarizations is desired, both for basic understanding and for use in calculating the ICRF-driven flows [1-3]. These notes will discuss numerical techniques (based on windowed Fourier transforms and wavelets) for the local mode analysis of 1D [3] and 2D [4, 5] toroidal ICRF field solutions, including mode-conversion scenarios, as part of the rf SciDAC project. The approach we have followed is to start with the simplest technique and gradually work towards more complicated methods when the simpler methods fail. In this section, we give a brief overview of the results and defer the details until later sections.

We illustrate these methods by considering the one-dimensional (1D) case where the function to be analyzed is a function f(x), represented by its values $f_i = f(x_i)$ on a grid of N spatial points x_i. The 1D transform specifies the mapping $f(x) \rightarrow F(k)$ where $k = k_x$ is also represented on a grid of N points. In the numerical examples below, we will analyze **E**(x) obtained from a fast wave (FW) to ion Bernstein wave (IBW) mode-conversion case computed by the 1D AORSA code with $x = R - R_0$ and $\mathbf{k} = k_x \mathbf{e}_x + (n/R) \mathbf{e}_z$, where R is the major radius of the tokamak and n is the toroidal mode number. This case uses parameters similar to those of the rf SciDAC benchmark 2D case [4, 5] and includes the important effect of the poloidal magnetic field on the wave physics.

The simplest approach is to use the usual **discrete Fourier transform** to resolve the wave propagation data into global k modes. This identifies all the relevant physical modes in the entire spatial domain of interest but does not yield any information as to their spatial location, nor does it yield insight into relationships among modes such as mode conversion.

To resolve this difficulty, one is led to consider the **Windowed Fourier Transform** (WFT) technique, in which the function E(x) to be transformed is multiplied by a window w(x). The best results are obtained using a window function that has no sharp discontinuities, e.g. a Gaussian $w(x) = \mathrm{Exp}[-(x-x_0)^2/(2x_w^2)]$, where x_0 and x_w are

the location and width of the window. The WFT method *with a constant window width* works well for a single wave or for the case of multiple waves with similar wavelengths, but it fails for the case of multiple waves with very different wavelengths. For example, the WFT method is not suitable for treating the mode conversion of a long wavelength fast wave (FW) to a short wavelength ion Bernstein wave (IBW). A large window is needed to resolve the wavelength (or k) of the FW but does a poor job in giving the spatial location of the IBW; a small window does a good job in resolving the IBW but does a poor job in resolving the FW wavelength.

An analysis of this problem shows that it stems from the need to minimize two conflicting types of errors: (1) the "Heisenberg" error $\Delta k_1 = C\pi/\Delta x$, where C is a constant of order unity and Δx is the size of the region in which the transform is carried out (here, the window width), and (2) the "non-local" or "gradient" error $\Delta k_2 \approx (\partial k/\partial x)\,\Delta x$, where k(x) is the local (eikonal) wavenumber. Note that the Heisenberg error goes away in the limit of a large window, whereas the gradient error goes away in the limit of a small window. So there is a competition between the two effects which produces an "optimal" window width such that the two errors are equal. The optimal window depends on the wavelength, i.e. $x_w = x_w(k)$. Thus, we must generalize the Windowed Fourier Transform technique to have a window width that scales with k.

The idea of a transform involving basis functions that are translated and scaled is well-known and such objects are called "wavelets" in the mathematical and engineering literature **[6-10]**. A variety of discrete and continuous wavelets have been developed for application in fields as diverse as signal processing, image compression, and scientific data analysis. In fact, the **Morlet wavelet [6]** is essentially equivalent to a windowed Fourier transform with a scaled Gaussian window, $x_w = c_0/k$, where c_0 is a constant. We implemented this technique and evaluated its usefulness for 1D mode conversion data. The scaled window is a big improvement over the WFT, but the scaling breaks down at k = 0. The infinite window width at k = 0 leads to large gradient error and false peaks in the spectrum. However, it is essential in treating the FW to IBW mode conversion problem that one resolve k's of both signs and therefore handle the behavior at k = 0.

We have developed a simple modification to the Morlet wavelet approach that allows us to keep its good features while still resolving the k = 0 region. We introduce another constant k_0 and scale the window width as $x_w = c_0/(k^2 + k_0^2)^{1/2}$ so that $x_w \rightarrow c_0/k_0$ as $k \rightarrow 0$. While this spoils the pure wavelet scaling in a small region, it permits us to obtain a physical answer over the whole x-k plane. For reasons given below, we refer to this approach as the "**k-wavelet**" method. It can be regarded as a WFT with a window width that depends on k, or as a Morlet wavelet with a suitable patch at k = 0. It should be emphasized that we do not need the "pure" wavelet scaling for our application. We are simply using the wavelet transform for visualization and for extracting the dispersion function k(x). We will show that the k-wavelet method provides a useful tool for graphically obtaining this information.

In the following sections, we present some of the technical details and results of the approaches described above. We conclude with a section describing some physics results which can be obtained by applying the k-wavelet technique.

B. Windowed Fourier Transforms

We begin with some definitions and conventions. Let f(x) be the function to be transformed and let it be defined and periodic on the interval $[x_a,x_b]$, i.e. $f(x_b) = f(x_a)$. The function is represented numerically on an equally-spaced grid of N points, $f_i = f(x_i)$ (i = 1, 2…N) where $x_i = x_a + (i - 1)\,\Delta x$ and $\Delta x = x_{i+1} - x_i = (x_b - x_a)/N \equiv 2L/N$. Here, L is the half-periodicity length, N is the number of sub-intervals and N+1 is the number of points on the full domain $[x_a, x_b]$. Note that the N+1st value is not needed because of periodicity, $f_{N+1} = f_1$. Also, let the set of coefficients $\{F_n\}$, n = 1…N, denote the discrete Fourier transform of $\{f_i\}$, i = 1 to N. Although the calculation is carried out on a discrete grid, we will sometimes adopt the continuum notation for simplicity of presentation; in this notation the forward transform is denoted by $f(x) \rightarrow F(k)$.

We define the forward and inverse Fast Fourier Transforms (FFT) by:

$$F_n = \frac{1}{N} \sum_{i=1}^{N} f_i \exp[-(i k_n x_i)] \quad , \tag{1}$$

$$f_i = \sum_{n=1}^{N} F_n \exp[i k_n x_i] \quad , \tag{2}$$

where $k_n = -k_{max} + (n - 1)\,\Delta k$; here, $\Delta k = \pi/L$ and $k_{max} = \pi/\Delta$ are the minimum and maximum wavenumbers, respectively, that can be resolved on the grid. Note that no restriction is made on the values of the endpoints $[x_a, x_b]$ and that we use a k-grid centered about k = 0. Both of these conventions differ from the ones used in *Mathematica*, but we have constructed our transform functions to do the appropriate transformations so that the conventions in Eqs. (1) and (2) are implemented in our *Mathematica* notebooks. The forward FFT transforms $f(x) \rightarrow F(k)$ so that all information is lost regarding the spatial location of a wave with a particular value of k. In other words, the k's are "global" rather than "local": they include all the values taken by the local k(x) on the interval $[x_a, x_b]$ covered by the transform. In order to get information on the local k, we turn to the Windowed Fourier Transform.

The Windowed Fourier Transform (WFT) of f(x) is obtained by taking the FFT of the product f(x) w(x), where w(x) is a window function that selects a subset of the total x interval. We have compared step-function and Gaussian windows and found that the latter yields better results because it has no discontinuities. Thus, we define the forward WFT by

$$F_n(x_0, x_w, k_n) = \frac{1}{N} \sum_{i=1}^{N} f_i \exp[-(i k_n x_i)] \exp\left[-\frac{(x_i - x_0)^2}{2 x_w^{\,2}} \right] \quad , \tag{3}$$

where the Gaussian $w(x_i)$ has two parameters: the window position x_0 and the window width x_w. If we take x_w to be constant in x and independent of k, then the WFT is a function of x_0 and k (or n); in continuum notation $F = F(x_0, k)$ with x_w as a parameter. For the applications of interest here, a plot of $F(x_0, k)$ contains in principle the desired physical information and we do not need the inverse WFT.

As an example to test the WFT method, we transform the rf electric field component $E_x(x)$ computed by the 1D AORSA code **[3]** for a DIII-D D(H) mode conversion reference case **[4, 5]**. The 1D equilibrium used here includes a model of the 2D poloidal magnetic field, which has an important effect on the wave physics. In particular, the wave physics above and below the midplane can be significantly different. Unless otherwise stated, the solution used here had parameters corresponding to a horizontal slice of the 2D equilibrium taken *above the midplane*. The present 1D transform analysis serves to illustrate the pros and cons of the various transform techniques.

Figure 1 shows 3D plots of the spectral power density $P(x_0, k) = |F(x_0, k)|^2$, where $f = E_x(x)$, for two values of the window width x_w. In Fig. 1(a) the large window width allows us to resolve the incident and reflected FW, but the mode-converted IBW is not spatially localized. In Fig. 1(b) the smaller window clearly shows the IBW, but the k-structure of the FW is lost. This example illustrates that a fixed window width can not simultaneously resolve and localize all wavelengths.

As discussed in Sec. A, the problem illustrated by Fig. 1 stems from the need to simultaneously minimize two conflicting types of errors: the "Heisenberg" error Δk_1 and the "non-local" or "gradient" error Δk_2, defined as

$$\Delta k_1 = C\frac{\pi}{\Delta x} \quad , \quad \Delta k_2 \approx \frac{\partial k}{\partial x}\Delta x \equiv k'(x)\Delta x \quad , \tag{4}$$

where $C = ½$ gives good estimates in our numerical tests, and we take $\Delta x \approx x_w$. Note that the Heisenberg error vanishes in the limit $x_w \to \infty$, whereas the gradient error is eliminated in the limit $x_w \to 0$. Thus, there is a competition between the two effects which produces an "optimal" window width. Defining the optimal x_w by the condition $\Delta k_1(x_w) = \Delta k_2(x_w)$ yields the following expression:

$$x_{w,opt} = \left(\frac{\pi}{2k'(x)}\right)^{1/2} \quad , \tag{5}$$

which implies that the optimal window width depends on k(x) and is therefore not constant in the (x, k) plane. This leads to the conclusion that we need to scale x_w with k. A useful starting point is to adopt a scaling along the lines suggested by the Heisenberg formula: $x_w \propto 1/k$. This scaling is naturally implemented by using wavelet transforms.

Fig. 1(a) $x_W = 0.25$ m

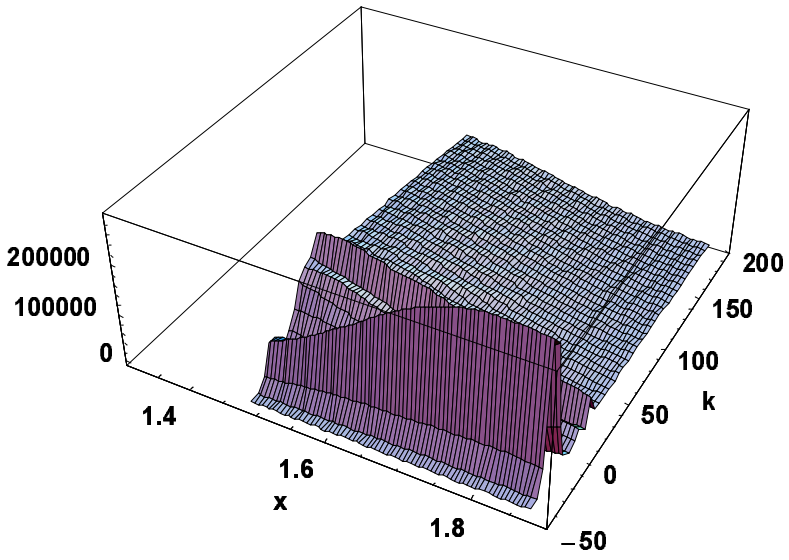

Fig. 1(b) $x_W = 0.05$ m

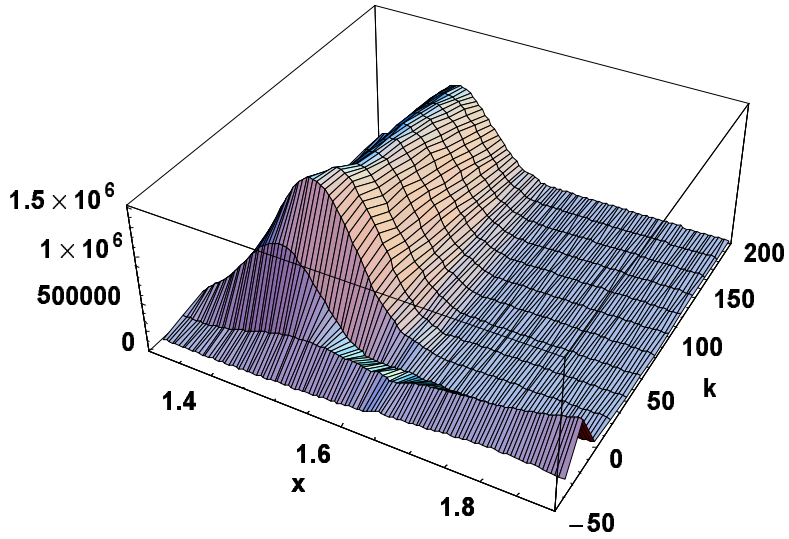

Fig. 1 Spectral power density $P(x_0, k)$ for the Fourier transform of $E_x(x)$ with two window sizes: (a) $x_W = 0.25$ m, and (b) $x_W = 0.05$ m. The label x refers to x_0 in this plot and the scale is in m; the scale of k is in m^{-1}.

C. Wavelet Transforms

Wavelet transforms [6-10] allow one to analyze a signal or a field pattern into both space and scale (time or space) simultaneously. As with other transforms, wavelets can be treated as either discrete or continuous functions of the independent variables. Important applications of wavelets include signal processing, image coding, and numerical analysis. One of the early workers in this field was Morlet, a French research scientist working on seismic data analysis, who developed continuous wavelet transforms of practical importance for processing scientific data. Wavelets have several potential applications of interest to fusion. For example, they may be a useful technique in reconciling two different aspects of turbulence: the turbulent cascade of wavenumber in Fourier space vs the formation of coherent spatial structures in physical space. Another important application is the one of interest here, viz. the description of wave propagation and mode conversion in complex media, where both the local wavenumber and its spatial location are important.

The essential difference between the Fourier and wavelet approaches lies in the spatial structure of the basis functions used in each case: spatially-extended trigonometric functions in the Fourier approach vs. spatially-localized functions in the wavelet approach. To take an example of present interest, the *Morlet wavelet* [6, 7] is given by

$$\Psi_M\left(\frac{x-x_0}{x_w}\right) = \exp\left[i\,c_0\left(\frac{x-x_0}{x_w}\right)\right]\exp\left[-\frac{(x-x_0)^2}{2\,x_w{}^2}\right] \quad , \tag{6a}$$

where c_0 is a parameter used to control the relative sizes of the Heisenberg and non-local errors. For present purposes, note that the Morlet function $\Psi_M(x)$ is spatially localized around $x = x_0$ by the Gaussian envelope with a half-width given by x_w. The relation to Windowed Fourier Transforms is made explicit by defining

$$x_w = c_0 / k \quad . \tag{6b}$$

Thus, the Morlet wavelet is equivalent to the Gaussian WFT with a window width $\propto 1/k$. Eq (6b) implies that k and x_w are equivalent parameters, so we will regard the wavelet as a function of (x_0, k) rather than (x_0, x_w). Finally, note that the conditions that (a) the eikonal (WKB) approximation is satisfied, and (b) the eikonal wavenumber is well resolved by the specified window width can be written as

$$kL_x \;>>\; kx_w = c_0 \;>>\; 1 \quad , \tag{7}$$

where L_x is the equilibrium scale length.

Before proceeding with the calculation, a brief discussion is useful to put this work in perpective relative to the wavelet literature. There are two broad classes of wavelets: discrete wavelet transforms (DWT) and continuous wavelet transforms (CWT). DWTs are constructed to have the properties of zero average ("admissibility"), orthogonality, and existence of an inverse transform. The "pyramidal algorithm" for DWTs [7-9] gives a fast inversion and is very useful for commercial applications, such as data compression and

signal processing, but it is not useful for extracting *phase information*, the application of interest here. To get complex phase information, one needs a complex CWT, which cannot be made orthogonal because the continuous wavelets overlap, giving redundant information. Continuous wavelet transforms can be implemented numerically on a grid, as done in the present work, but this technique should not be confused with true discrete wavelet transforms, such as the Haar or Daubechies wavelets **[8]**. Thus, the present application of wavelets is somewhat non-standard in that it is meant to extract phase information (in addition to the usual scale information), in a situation where there are well-defined waves. For this application, we are only interested in using the *forward* wavelet transform and do not need to be able to invert the transform. The other DWT conditions (admissibility, orthogonality) also do not apply here.

For the present application, we apply the Morlet wavelet on the spatial grid defined above and define the wavelet transform $f(x) \rightarrow W(x_0, k)$ as

$$W(x_0,k) = \frac{1}{N}\sum_{i=1}^{N} f_i \, \Psi^*\left(\frac{x_i - x_0}{x_w}\right) = \frac{1}{N}\sum_{i=1}^{N} f_i \exp\left[-ic_0\left(\frac{x_i - x_0}{x_w}\right)\right]\exp\left[-\frac{(x_i - x_0)^2}{2{x_w}^2}\right] , \quad (8)$$

where the 1/N factor was chosen to give the same normalization as in the WFT case and we henceforth drop the subscript M on the wavelet function.

Equation (8) implies that the desired transform is the convolution of f(x) with $\Psi[(x - x_0)/x_w]$. If we were to compute this in x-space for each value of k on the k-grid, the required number of computations would scale like N^2, which is inefficient. The *convolution theorem* can be used to recast the convolution into k-space FFTs **[10]**. The resulting calculation scales like N ln N, because for each value of k we obtain the entire dependence on x_0. Moreover, the convolution is easy to code in *Mathematica* and executes quickly using the built-in FFTs. Thus, we re-write Eq. (8) as

$$W(x_0,k) = \frac{1}{N}\Im^{-1}\left(\Im[f(x)]\,\Im\left[\Psi^*\left(\frac{x - x_0}{x_w}\right)\right]\right) , \quad (9)$$

where $\Im[f(x)]$ denotes the forward Fourier transform of f(x), $\Im^{-1}$ denotes the inverse Fourier transform, and the k dependence on the rhs of Eq. (9) is implicit through the relation $k = c_0/x_w$. In the implementation of Eq. (9), care must be taken to ensure that $\Psi[(x - x_0)/x_w]$ is *periodic*, i.e. that the window function "wraps around" the boundaries of the x interval $[x_a, x_b]$.

Aside: This is easily implemented in *Mathematica* by computing the list $\{w_i\}$, i = 1 to N, where $w_i = \Psi[(x_i - x_0)/x_w]$ with x_0 chosen to lie in the interior of the interval, e.g. $x_0 = (x_a+x_b)/2$; then we rotate this list N/2 times to get the wavelet function corresponding to $x_0 = x_a$ with the function properly wrapped around the x boundaries. The result of evaluating

the rhs of Eq. (9) for the latter form of the wavelet function yields a list whose first element corresponds to $x_0 = x_a$ and whose last element corresponds to $x_0 = x_b$, which is gridded representation of the desired function $W(x_0, k)$.

It turns out that there is a problem with applying the Morlet transform to the ICRF solution which can be illustrated by plotting the wavelet spectral power density, $P(x_0, k) = |W(x_0, k)|^2$. A 3D plot of $P(x_0, k)$ is shown in **Fig. 2** for the case $c_0 = 6$ with $f(x) = E_x(x)$. One sees an improvement over the WFT technique in that the wavelet method can resolve both the FW and IBW simultaneously. However, there is a problem near $k = 0$ associated with the singularity in Eq. (7): $x_w \to \infty$ as $k \to 0$, which introduces unphysical oscillations in the spectrum $P(k)$. As the window scale increases, the gradient error becomes very large and causes the extra peaks. For ICRF calculations with incident and reflected waves we must modify this technique to eliminate the $k = 0$ singularity. This is discussed in the next section.

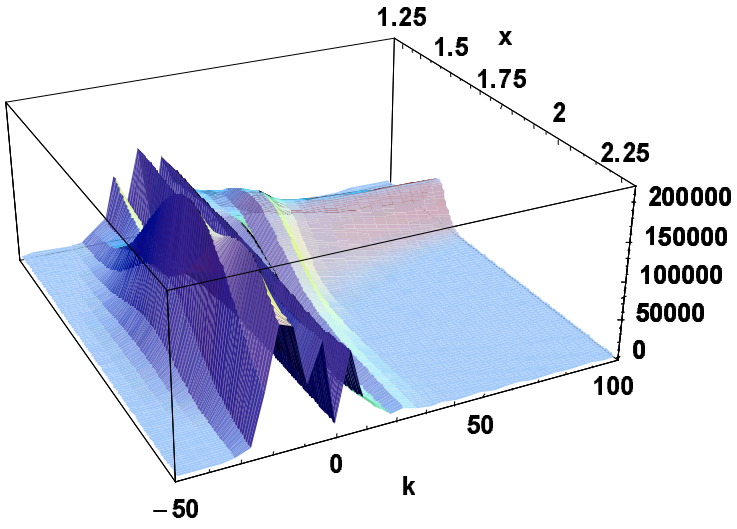

Fig. 2 Spectral power density $P(x_0, k)$ for the Morlet wavelet transform of $E_x(x)$ using the scaling $x_w = c_0/k$ with $c_0 = 6$. Note the rapid oscillations near $k = 0$ which are unphysical. The label x refers to x_0 in this plot and the scale is in m; the scale of k is in m^{-1}.

D. Modified Wavelet Transforms

In this section we discuss a modified wavelet transform technique which preserves the scaling of the Morlet wavelet at large k but satisfies two additional conditions: (i) it describes windowed plane waves ~ exp[i kx] for all k, and (ii) it has a finite window width (spatial scale) x_w at k = 0. Both of these conditions are satisfied by the following minor modification of the Morlet wavelet which we call the "*k-wavelet*":

$$\Psi[k(x-x_0)] = \exp[i\,k(x-x_0)]\,\exp\left[-\frac{k^2(x-x_0)^2}{2\,k^2 x_w^{\,2}}\right] , \qquad (10a)$$

$$x_w = \frac{c_0}{\sqrt{k^2 + k_0^{\,2}}} , \qquad (10b)$$

where k_0 is a parameter that determines the wavelet scale at k = 0: $x_w(k = 0) = c_0/k_0$. Note that Eq. (10b) is the needed generalization of Eq. (7) to prevent the k = 0 singularity. This form also preserves the correct phase information for both signs of k.

Strictly speaking, the function in Eq. (10) is not a *pure* Morlet wavelet because the wavelet scaling is not preserved for small k, i.e. kx_w is not a constant as $k \to 0$. In this limit, it reduces to a Gabor windowed Fourier transform. One could equally well regard this as a modified WFT approach with a window scaled according to Eq. (10b) and using the convolution technique of Eq. (9). However, it is so close to the spirit of the wavelet approach that we prefer to view Eq. (10) as a modified wavelet. Since it is a hybrid of the ***Gabor transform*** as $k \to 0$ and the ***Morlet wavelet*** as $k \to \infty$, one could also refer to it as a "*Gabor-Morlet transform*".

Substituting Eq. (10) into Eq. (9) yields the modified k-wavelet transform $W(x_0, k)$. A 3D plot of the wavelet spectral power density, $P(x_0, k) = |W(x_0, k)|^2$, is shown in **Fig. 3** (see next page) for the case $c_0 = 5$, $k_0 = 40$ m^{-1}. Here, $W(x_0, k)$ is the wavelet transform of the rf field component $E_x(x)$ and $k = k_x$. One sees the incident and reflected fast waves at ±20 m^{-1} and the mode-converted IBW propagating at large k. The behavior near k = 0 is now physical.

It is interesting to compare the modified wavelet approach with the original windowed Fourier transform results. This is shown in **Fig. 4** (see next page), where we compare contour plots of the WFT analysis using $x_w = 0.25$ m with the k-wavelet case of Fig. 3. We see that the resolution of the long- wavelength FW is comparable in the two plots, but the wavelet approach has much better spatial resolution of the short-wavelength IBW at large k.

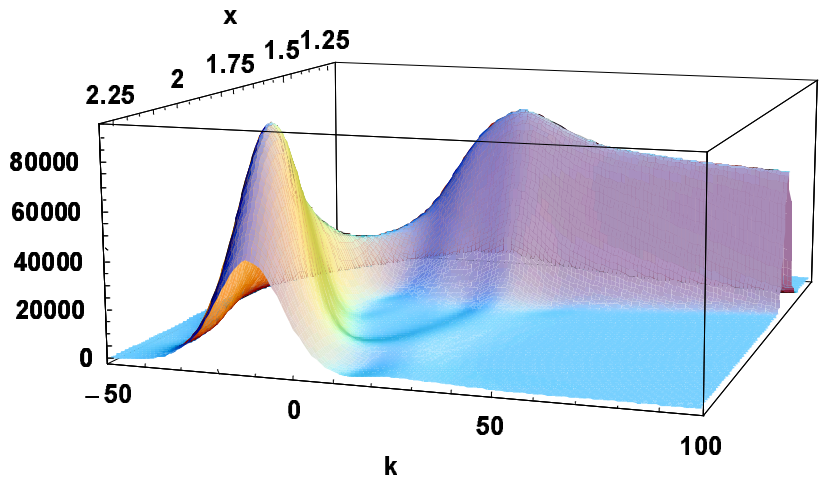

Fig. 3 Spectral power density $P(x_0, k)$ for the k-wavelet transform of $E_x(x)$ using the scaling $x_w = c_0/(k^2 + k_0^2)^{1/2}$ with $c_0 = 5$ and $k_0 = 40$ m^{-1}. Note that the behavior near k = 0 is now physical and all waves are resolved. The label x refers to x_0 in this plot and the scale is in m; the scale of k is in m^{-1}.

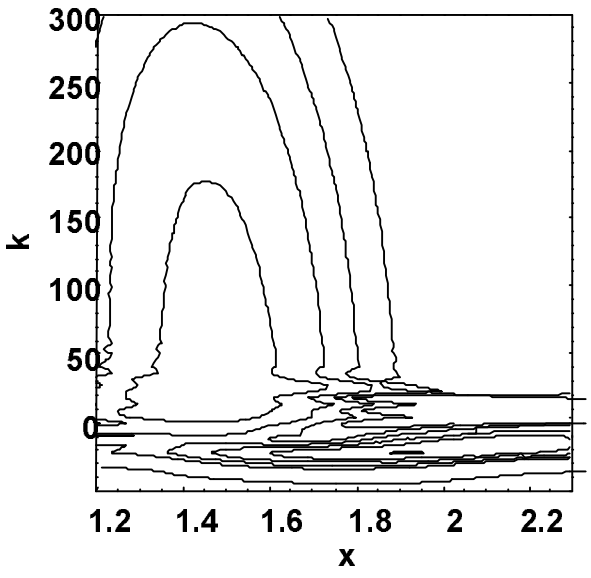

Fig. 4(a)

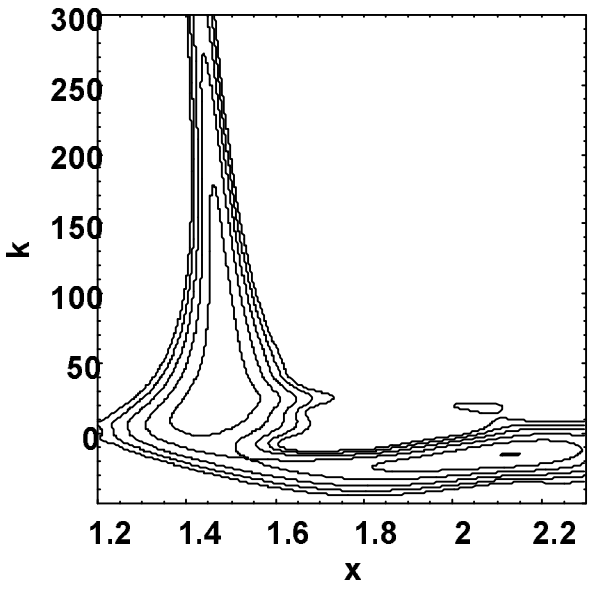

Fig. 4(b)

Fig. 4 Contour plots of the spectral power density $P(x_0, k)$ for (a) the windowed Fourier transform of $E_x(x)$ with $x_w = 0.25$ m, and (b) the k-wavelet transform of $E_x(x)$ using the scaling $x_w = c_0/(k^2 + k_0^2)^{1/2}$ with $c_0 = 5$ and $k_0 = 40$ m^{-1}. Note

that the wavelet approach gives much better resolution of the IBW. The label x refers to x_0 in this plot and the scale is in m; the scale of k is in m^{-1}.

E. Physics Applications of the modified Wavelet Transform

Now that we have a working method, we can use it to extract useful physical information from the computed rf fields. In this section, we explore some of the applications of the k-wavelet method and generalize our discussion to include all components of the rf field.

The contour plot in Fig. 4(b) provides information on the dependence $k = k_x(x)$ for the incident and reflected FW and the mode-converted IBW. We see the incident FW propagate to the left with $k < 0$ and encounter the mode-conversion surface near $x = 1.5$, giving rise to a reflected FW with $k > 0$ (visible as small "fingers" on the plot) and the IBW that propagates to the left (smaller x) with a positive k. Thus, this plot illustrates that the IBW is a backward-propagating wave. To get more quantitative information, it is useful to examine vertical cuts of the spectral power density $P(k) = |W(x_0, k)|^2$ at fixed x_0. **Figure 5** compares P(k) at $x_0 = 1.75$ m in the outer plasma (dashed curve) and $x_0 = 1.6$ m near the mode conversion layer (solid curve). The incident and reflected FW peaks are located at $k = \pm 25$ m^{-1} and one sees the decay of the incident (reflected) wave as it propagates to smaller (larger) x.

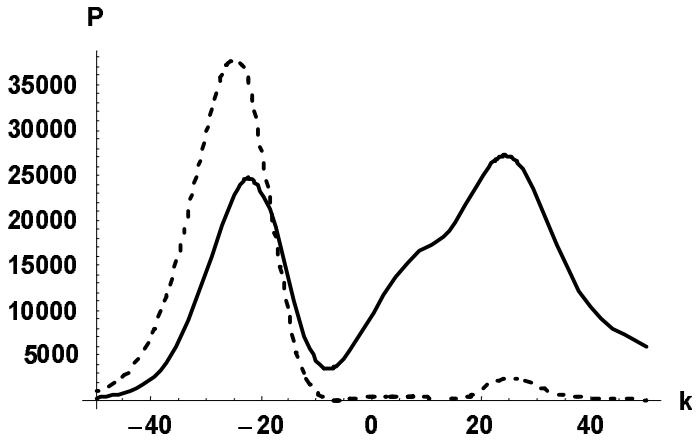

Fig. 5 Plot of the wavelet spectral power density P(k) at fixed x_0 obtained by the k-wavelet transform of $E_x(x)$ for the same parameters as in Fig. 3(b). The dashed curve corresponds to $x_0 = 1.75$ m, located in the outer plasma; the solid curve corresponds to $x_0 = 1.6$ m, near the mode conversion layer.

So far, we have only applied the wavelet transform to the x-component of the rf field, $E_x(x)$. Now we generalize the treatment to the other field components and define the spectral power density $P_\alpha(x_0, k) = |W_\alpha(x_0, k)|^2$, where W_α is the k-wavelet transform of $E_\alpha(x)$.

To test the quantitative accuracy of the wavelet analysis of the AORSA numerical solution, in **Fig. 6** we compare the contour plot of $P_\perp(x_0, k) = P_x(x_0, k) + P_y(x_0, k)$ (shown

in red) with the 1D hot-plasma dispersion relation (heavy blue lines). As an aside, we mention that two improvements are made in Fig. 6 as compared with Fig. 4b. More contours are used to show the details more clearly, and we plot $P_{\perp}(x_0, k)$ rather than $P_x(x_0, k)$. Note that $P_{\perp}(x_0, k)$ is a measure of the intensity of the wavelet transform of $E_{\perp}(x) = (E_x^2 + E_y^2)^{1/2}$ and is probably a more physical quantity to plot, since the E_y component plays an important role for the FW.

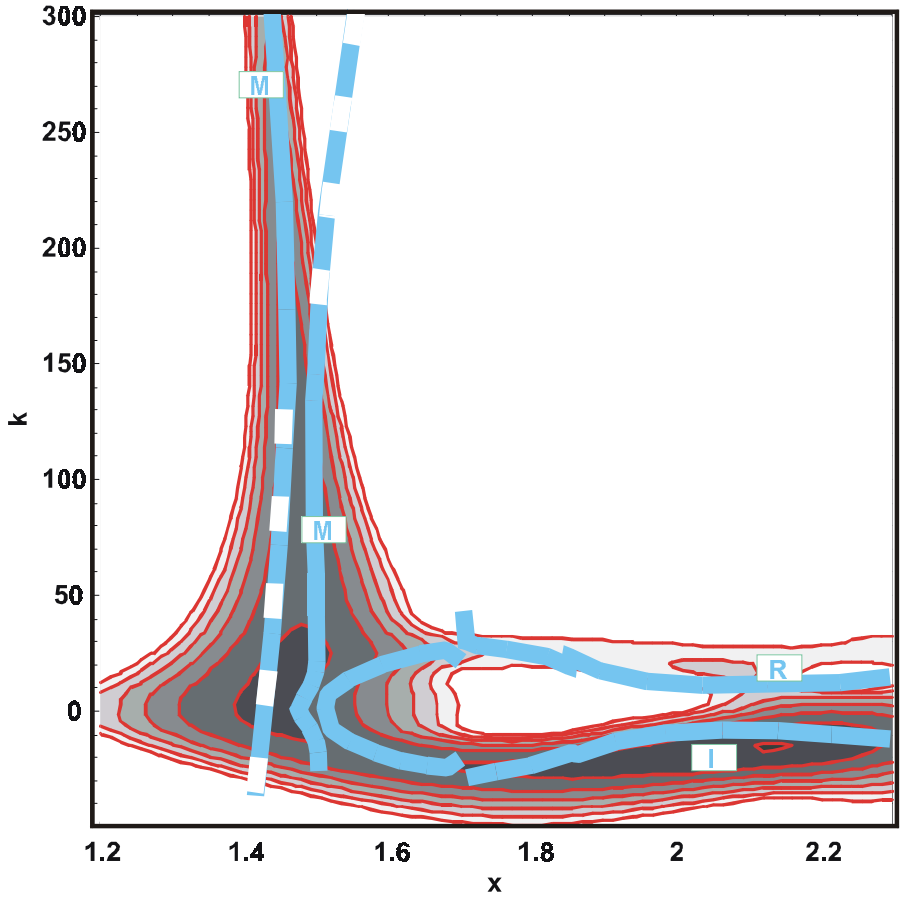

Fig. 6 Comparison of the k-wavelet spectral power density $P_{\perp}(x_0, k)$ (red contour lines) with the hot-plasma dispersion relation (blue lines). The solid (dashed) blue lines depict propagating (heavily damped) modes. The label x refers to x_0 in this plot and the scale is in m; the scale of k is in m^{-1}.

There are several points of agreement between the analytic dispersion relation and the contour plot. First, we note that the maximum positive and negative values of k for the incident and reflected fast waves agree well with the wavelet contours; the regions where the dispersion relation give $k \rightarrow 0$ do not agree as well, probably because the eikonal approximation used in the dispersion relation breaks down in that region. Second, there is good agreement on the location of the mode conversion surface near x = 1.5 m. Finally,

we compare the two branches of the dispersion relation for x < 1.6 m (vertical blue lines) with the IBW contours. On each branch there is a region where the mode is heavily damped (dashed blue line) and a region where the mode propagates (solid blue line). The transmitted wave energy tunnels from one branch to the other. Again, the analytic results show good agreement with the wavelet contours. We conclude that the k-wavelet transform is useful for obtaining quantitative information about the spatial dependence of the wavenumber.

Another important generalization is to include both amplitude and wave polarization information in the 3D plots. As this technique is so useful, we make a short digression from the physics to document how this is done using the shading and color capabilities of the *Mathematica* 3D plotting functions. We define an amplitude function A, saturation function S, and hue function H in terms of two input functions f(x,k) and g(x,k) by

$$A[f(x,k),g(x,k)] = \frac{f+g}{\mathrm{Max}[f+g]} \quad , \tag{11a}$$

$$S[f(x,k),g(x,k)] = \mathrm{Min}\left[\alpha A^{\nu}, 1\right] \quad , \tag{11b}$$

$$H[f(x,k),g(x,k)] = C_H\left(\frac{2}{\pi}\mathrm{Tan}^{-1}(g/f) + \delta\right) \quad , \tag{11c}$$

In Eq. (11a), the maximum is taken over all x and k. The parameters α and ν in Eq. (11b) are used to adjust the saturation level and to determine how many contours are illuminated. Finally, the parameters C_H and δ in Eq. (11c) determine a linear mapping between the ratio g/f and the angular coordinate in the color wheel. Varying these parameters determines the color palette and its mapping onto the physical quantity g/f. The *Mathematica* 3D plot function takes two functions as input, a height function and a shading function; we take A(x, k) to be the height function and Hue[H(x,k), S(x,k), 1] to be the shading function. Here, Hue is the *Mathematica* function to specify color values, and it accepts input in the *hsb* (hue, saturation, and brightness) format with h, s, and b each between 0 and 1; larger values of h are treated cyclically.

Plots illustrating the wave polarization are shown in **Fig. 7** for the choice $f = P_y(x_0, k)$ and $g = P_x(x_0, k)$ with plotting parameters $\alpha = 1$, $\nu = 0.1$, $C_H = 0.7$, and $\delta = 1.8$. This produces a color palette running from light green (for $P_x/P_y \to 0$) through light blue, dark blue, lavender, to red (for $P_x/P_y \to \infty$). Note that here the amplitude is the normalized version of $P_\perp(x_0, k)$. In Figs. 7(a) and (b) we show two views of the 3D plot, with and without reference grid lines. In each case, the fast wave is blue, indicating moderate E_x, but the IBW is red, showing that E_x dominates. The mode conversion region has a complicated structure with regions of smaller E_x/E_y than either the incident FW or the mode converted IBW.

Fig. 7(a) front view (without grid lines):

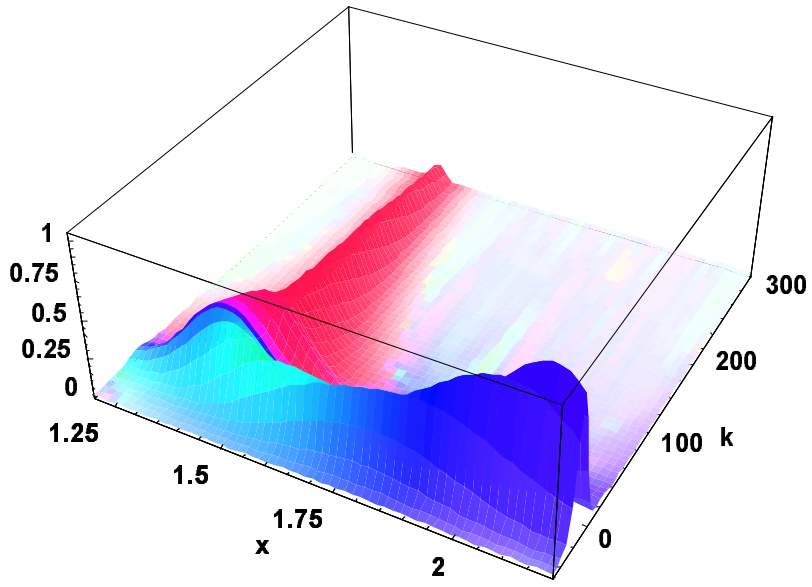

Fig. 7(b) back view (with grid lines):

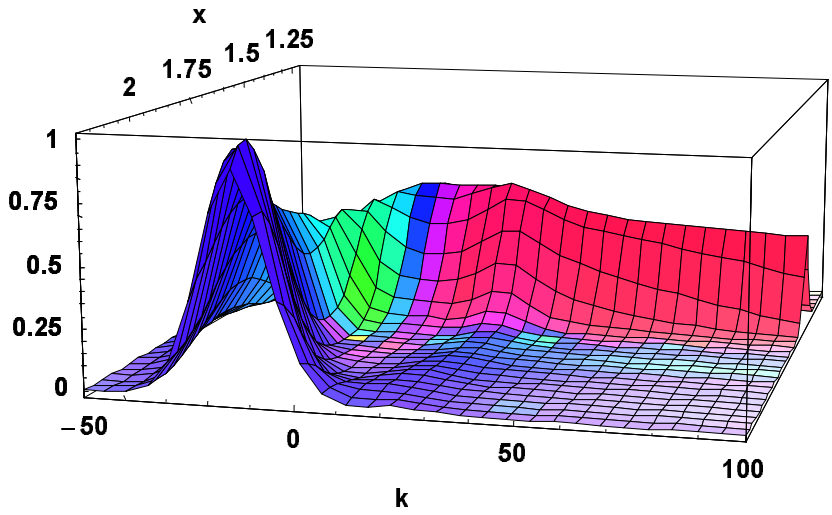

Fig. 7 K-wavelet transform spectral power density $P_{\perp}(x_0, k)$ of the rf electric field using the same parameters as Fig. 3. Here the color palette indicates the *linear* wave polarization E_x/E_y as explained in the text. The label x refers to x_0 in this plot and the scale is in m; the scale of k is in m^{-1}.

Figure 8 uses the same palette as in Fig. 7 to illustrate the wave polarization in terms of the left- and right-circularly-polarized fields, $E_L = (E_x + iE_y)/\sqrt{2}$ and $E_R = (E_x - iE_y)/\sqrt{2}$, which are the characteristic polarizations of the slow and fast waves, respectively. The palette mapping onto E_R/E_L extends from light green ($E_L >> E_R$) through blue ($E_L \approx E_R \Rightarrow$ linear polarization) to red ($E_L << E_R$). Thus, Fig. 8 clearly illustrates the transition from the right-circularly-polarized FW to the linearly-polarized IBW. This figure also shows a small region of significant left-hand polarization (light green) near the mode-conversion surface.

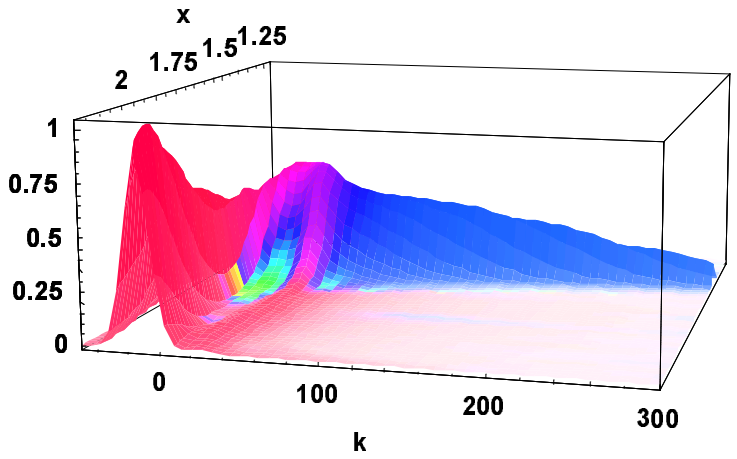

Fig. 8 K-wavelet transform spectral power density $P_\perp(x_0, k)$ of the rf electric field using the same parameters as Fig. 3. Here the color palette indicates the *circular* wave polarization E_R/E_L as explained in the text. The label x refers to x_0 in this plot and the scale is in m; the scale of k is in m^{-1}.

In **Fig. 9** we use a modified palette to illustrate the subtle change of polarization near the H minority cyclotron resonance at x = 1.7 m. By increasing C_H to 20, we magnify the palette to show small changes in polarization. (Thus, the mapping of colors onto E_R/E_L are quite different in Figs. 8 and 9.) This reveals some structure in Fig. 9 near the minority cyclotron resonance.

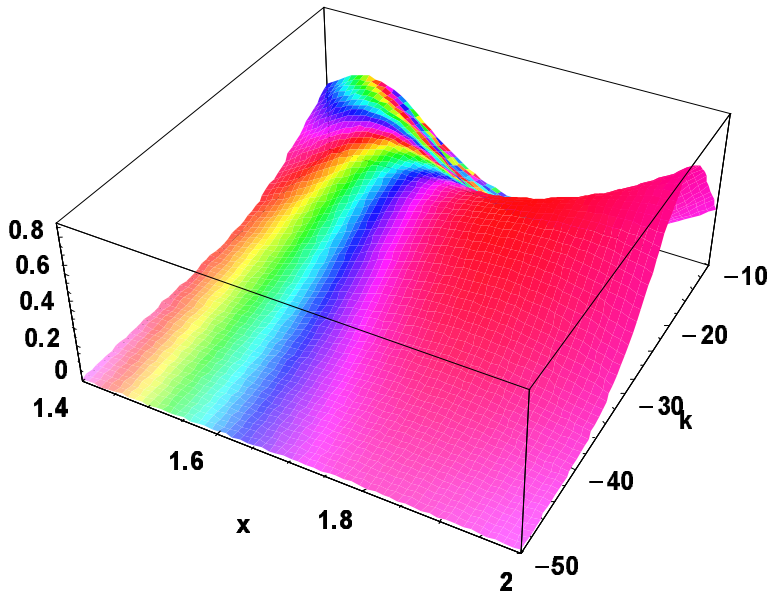

Fig. 9 K-wavelet transform spectral power density $P_{\perp}(x_0, k)$ of the rf electric field using the same parameters as Fig. 3. Here the color palette has been modified to show small changes in the wave polarization E_R/E_L and is used to illustrate the wave structure near the minority cyclotron resonance. The label x refers to x_0 in this plot and the scale is in m; the scale of k is in m^{-1}.

Finally, we use the k-wavelet transform to illustrate an interesting and important physics point that has emerged from the recent studies **[13]** of mode conversion using the 2D AORSA code. It has been shown that ICRF mode conversion is sensitive to the poloidal magnetic field, which determines whether the fast wave converts to an ion Bernstein wave (IBW) or an ion cyclotron wave (ICW). For the base case studied here, the mode conversion yields different daughter waves above and below the midplane. In **Fig. 10**, we compare two horizontal slices to illustrate this effect. Above the midplane [Fig. 10(a)] the incoming FW converts to a backward-propagating IBW, as also seen in the previous figures. Below the midplane [Fig. 10(b)] the FW converts to a forward-propagating ICW.

Fig. 10 (a) Above the midplane (b) Below the midplane

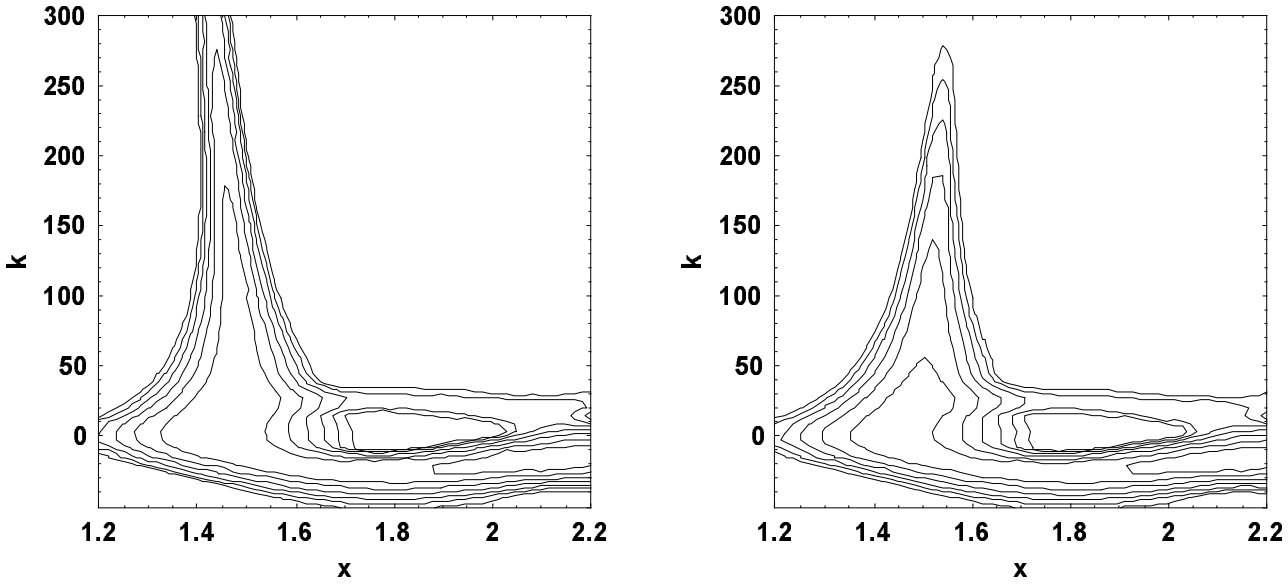

Fig. 10 K-wavelet transform spectral power density $P_{\perp}(x_0, k)$ of the rf electric field for horizontal slices (a) above the midplane, and (b) below the midplane. The label x refers to x_0 in this plot and the scale is in m; the scale of k is in m^{-1}.

F. Conclusions

In this paper, we have defined a modified transform that has desirable properties for the local analysis of waves in plasmas. This transform has the following limiting cases: as $k \rightarrow 0$ it reduces to the windowed Fourier transform of Gabor; in the limit of large k, the transform becomes the well-known Morlet wavelet. The name "k-wavelet" introduced here was meant to suggest that the wavelet properties depend on k, because the low-k Gabor transform does not satisfy the usual self-similar wavelet scaling (in which all wavelet functions are obtained by translation and dilation of the same mother wavelet) [7]. Thus, a more accurate description of our modified transform would be to call it the "*Gabor-Morlet transform*."

We have shown that the “k-wavelet” or "Gabor-Morlet" transform can provide a useful diagnostic for wave properties in complex situations. This includes situations such as mode conversion where multiple waves with vastly different wavelengths are present simultaneously. For 1D numerical solutions, the wavelet technique has been shown to provide quantitative information on the dispersion [e.g. $k_x(x)$ at fixed ω] and polarization

[e.g. $E_L(x)/E_R(x)$] of each mode in the plasma. The methods used here can also be generalized to obtain the two-dimensional wavevector $\mathbf{k}_\perp = (k_x, k_y)$ for 2D rf field solutions, $\mathbf{E} = \mathbf{E}(x,y)$. However, the 1D analysis illustrated here is expected to be qualitatively valid if $k_y << k_x$. The Fourier and wavelet techniques developed here may also be useful in analyzing turbulent and coherent structures (e.g. "blob" transport **[11, 12]**) in computer simulations and experimental data for comparison with theoretical predictions.

References

1. E. F. Jaeger, L. A. Berry, and D. B. Batchelor, Phys. Plasmas **7**, 641 (2000); and references therein.
2. J. R. Myra and D. A. D'Ippolito, Phys. Plasmas **7**, 3600 (2000); Phys. Plasmas **9**, 3867 (2002); and references therein.
3. E.F. Jaeger, L. A. Berry, and D. B. Batchelor, Phys. Plasmas **7**, 3319 (2000).
4. E.F. Jaeger, L. A. Berry, E. D'Azevedo, D. B. Batchelor, and M. D. Carter, Phys. Plasmas **8**, 1573 (2001).
5. D. B. Batchelor, E. F. Jaeger et al., DOE SciDAC project "Numerical Calculations of Wave Plasma Interactions in Multi-dimensional systems," see description and plots for this baseline case at: http://www.ornl.gov/fed/scidacrf/blc/InitialbaselineEFJ.pdf .
6. "Sampling theory and wave propagation," J. Morlet, NATO ASI, Vol. F1, *Issues on Acoustic Signal/Image Processing and Recognition*, ed. C. H. Chen (Springer, Berlin, 1983); "Decomposition of Hardy functions into square integrable wavelets of constant shape," A. Grossmann and J. Morlet, SIAM J. Math. **15**, 723 (1984).
7. "Wavelet transforms and their applications to turbulence," M. Farge, Annu. Rev. Fluid Mech. **24**, 395 (1992).
8. "An Introduction to Wavelets," A. Graps, IEEE Computational Science and Engineering, vol. 2, (1995); also available at http://www.amara.com/IEEEwave/IEEEwavelet.html .
9. "Wavelets for kids – A Tutorial Introduction," B. Vidakovic and P. Mueller, December, 1994; available at http://www.isye.gatech.edu/~brani/wp/kidsA.pdf .
10. "A Practical Guide to Wavelet Analysis," C. Torrence and G. Compo, Bulletin of the American Meteorological Society **79**, 61 (1998).
11. S. I. Krasheninnikov, Phys. Lett. A **283**, 368 (2001).
12. D. A. D'Ippolito, J. R. Myra and S. I. Krasheninnikov, Phys. Plasmas **9**, 222 (2002).
13. E.F. Jaeger, L. A. Berry, D. B. Batchelor, P. T. Bonoli, C. K. Phillips, R. J. Dumont, and D. N. Smithe, presented at the *44th APS-DPP Meeting*, Orlando, FL, November 11-15, 2002, paper BP1.074.